Strain-driven chiral phonons in two-dimensional hexagonal materials

Habib Rostami,[1] Francisco Guinea,[2,3,4] and Emmanuele Cappelluti[5]

[1]*Nordita, KTH Royal Institute of Technology and Stockholm University, Hannes Alfvéns väg 12, 10691 Stockholm, Sweden*

[2]*Imdea Nanoscience, Faraday 9, 28047 Madrid, Spain*

[3]*Donostia International Physics Center, Paseo Manuel de Lardizábal 4, 20018 San Sebastián, Spain*

[4]*Ikerbasque. Basque Foundation for Science, 48009 Bilbao, Spain*

[5]*Istituto di Struttura della Materia-CNR (ISM-CNR), 34149 Trieste, Italy*

(Received 22 January 2022; revised 4 May 2022; accepted 16 May 2022; published 26 May 2022)

Hexagonal two-dimensional materials with broken inversion symmetry (as BN or transition metal dichalcogenides) are known to sustain chiral phonons with finite angular momentum, adding a further useful degree of freedom to the extraordinary entangled (electrical, optical, magnetic, and mechanical) properties of these compounds. However, because of lattice symmetry constraints, such chiral modes are constrained to the corners of the Brillouin zone, allowing little freedom for manipulating the chiral features. In this paper, we show how the application of uniaxial strain leads to the existence of unique chiral modes in the vicinity of the zone center. We also show that such strain-induced chiral modes, unlike the ones pinned at the K points, can be efficiently manipulated by modifying the strain itself, which determines the position of these modes in the Brillouin zone. The present paper results add a technique for the engineering of the quantum properties of two-dimensional lattices.

DOI: 10.1103/PhysRevB.105.195431

I. INTRODUCTION

The possibility of exfoliating and growing two-dimensional materials at the atomically thin level [1–7] has paved the way for designing flexible systems with a striking capability of converting mechanical deformations into electronic or optical properties [8–11]. In the paradigmatic case of graphene, as well as for other systems with a hexagonal/triangular lattice, like h-BN or transition metal dichalcogenides (TMDs), the entanglement between electronic properties and the lattice is enriched by the presence of two inequivalent sublattices. Note that the crystal structure of single-layer MX_2 TMDs can be viewed from the top as a hexagonal lattice, i.e., a triangular lattice with a proper basis defined by M on sublattice A and the top/bottom X atoms on sublattice B. Such an additional degree of freedom is conveniently cast in terms of a *spinor* vector [12] which, in the momentum space, is reflected in the occurrence of two inequivalent valleys at the high-symmetry points K, K′. The possibility of tuning the physical properties of two valleys, and encoding there quantum information, has given rise to the concept of *valleytronics* [13,14]. A peculiar feature of the graphene, BN, and TMDs, due to their hexagonal lattice symmetry, is that each valley is characterized by a remarkable chiral structure, with opposite chirality of opposite K points. Furthermore, the breaking of inversion symmetry leads to a gap opening which is accompanied by the onset of a finite Berry curvature [15–18].

Lattice modes (phonons) represent a further degree of freedom that can convey interesting quantum phenomena. Moreover, it was recently shown that phonons in a hexagonal lattice with mass disproportion (e.g., BN or TMDs) also

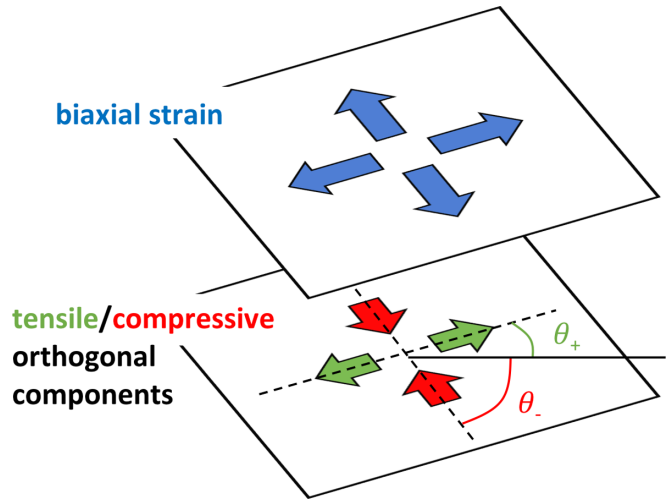

FIG. 1. Decomposition of a generic strain tensor in two main components: a biaxial strain and a strongly anisotropic term with two orthogonal components, with equal strain strength but opposite character (tensile versus compressive). In the sketch, the relevant angles θ_+, θ_- for the tensile and compressive components are defined.

can carry an angular momentum and sustain *chiral* modes in the same way as electrons do [19–28]. Manipulating the properties of the lattice modes can thus provide an alternative and complementary scenario with promising perspectives for writing-in/reading-out quantum information.

The phonon dispersion of graphene presents a Dirac structure at the K, K′ points in the subspace of the acoustic/optical modes. In a similar way to the electronic Dirac states, a key role is played by the breaking of inversion symmetry, driven by the mass disproportion, and leading to the opening of a gap at K, K′. Just as for the electronic degrees of freedom, as pointed out in the seminal work in Ref. [20], due to the crystal symmetry, such chiral phonons are pinned at the high-symmetry points K, K′. Symmetry arguments predict that chirality concepts could apply as well at the zone-center Γ point, where the degeneracy of the transverse and longitudinal modes in the Cartesian basis can be as well expressed in terms of two (degenerate) chiral modes with opposite signs. Such opportunity is, however, not particularly useful for practical purposes since the intrinsic degeneracy of the two modes does not allow for a feasible manipulation of the chiral degree of freedom. Degeneracy splitting is thus a necessary requirement. Within this perspective, applying a real magnetic field, through the electron-phonon coupling, has been shown to induce a chiral lattice polarization [29], whereas the uniaxial strain has been discussed to be detrimental with respect to chirality since it favors linear polarization [30–33]. Finding the way of sustaining chiral modes in the closeness of the Γ point is thus of the highest relevance since it could open the way for a direct probe of chiral phonons by means of optical means at $\mathbf{q} \approx 0$.

In this paper, we demonstrate chiral phonons that can be conveniently generated and engineered close to the Γ point in the optical branches of hexagonal systems with sublattice inequivalence (e.g., h-BN, TMDs, gapped graphene) by applying a simple homogeneous anisotropic strain. Furthermore, we show that such chiral modes appear in pairs of opposite chirality and, unlike the chiral modes constrained at the K, K′ point, the net momentum for each chirality does not average to zero. The closeness of the chiral phonons to the Γ point on the other hand, opens the way for an optical probe.

II. ANISOTROPIC STRAIN AXES

Before analyzing the effects of anisotropic strain on the properties of the lattice dynamics at a microscopic level, we introduce a few useful notations for characterizing the strengths and axes of anisotropic strains. We consider the tensor in a Cartesian basis for a generic anisotropic strain,

$$\boldsymbol{\varepsilon} = \begin{bmatrix} \varepsilon_{xx} & \varepsilon_{xy} \\ \varepsilon_{xy} & \varepsilon_{yy} \end{bmatrix}, \tag{1}$$

where $\varepsilon_{ij} = (\partial_i u_j + \partial_j u_i)/2$, and where $\partial_i u_j$ is derivative of the *strain* lattice displacement u_j along the direction i [34]. On the general ground, the above tensor can be viewed as a superposition of an isotropic biaxial average strain,

$$\varepsilon_0 = (\varepsilon_{xx} + \varepsilon_{yy})/2, \tag{2}$$

plus an anisotropic strain with a tensile ($\Delta\varepsilon/2 > 0$) and a compressive ($-\Delta\varepsilon/2 < 0$) orthogonal component, where

$$\Delta\varepsilon = \sqrt{(\varepsilon_{xx} - \varepsilon_{yy})^2 + 4\varepsilon_{xy}^2}. \tag{3}$$

The tensile and compressive strains are aligned along the angles [35]:

$$\theta_+ = \theta_- + \frac{\pi}{2} = \frac{1}{2}\arctan\left(\frac{2\varepsilon_{xy}}{\varepsilon_{xx} - \varepsilon_{yy}}\right). \tag{4}$$

The respective strengths of the strain along such characteristic axes are thus obtained as

$$\varepsilon_\pm = \varepsilon_0 \pm \Delta\varepsilon/2. \tag{5}$$

The biaxial, tensile, and compressive components of the uniform strain are visualised in Fig. 1.

III. LATTICE DYNAMICS MODELING

A. Unstrained case

We consider the paradigmatic case a bipartite hexagonal lattice with two different masses M_1, M_2 in the two sublattices. We set the armchair direction along the x axis, and we denote as atom 1 the atom on the left of the x-axis bond [see Fig. 2(a)]. In the absence of strain, given the interatomic

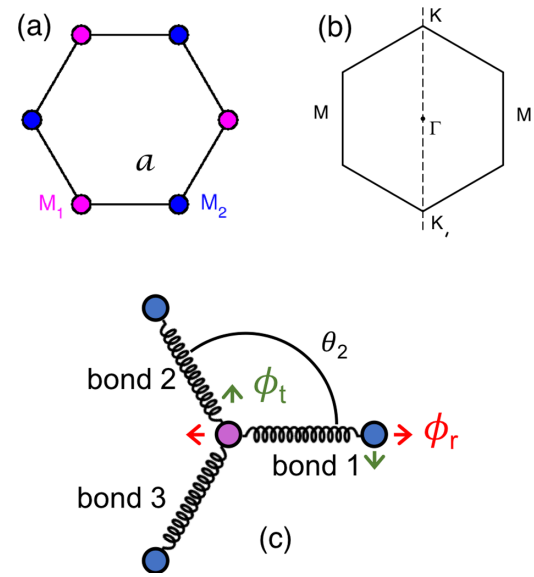

FIG. 2. (a) Lattice structure and (b) Brillouin zone of a bipartite hexagonal lattice. Atoms on sublattice 1 have masses M_1, atoms on sublattice 2 have masses M_2. (c) Sketch of the relevant geometry and force-constant parameters employed in the present modeling. Purple balls represent atoms on sublattice 1, blue balls atoms on sublattice 2. Each atom on sublattice 1 is connected to three nearest-neighbor atoms on sublattice 2 through three geometrically different bonds. The force-constant ϕ_r rules the elastic properties of the lattice displacement along the bond direction, ϕ_t the elastic properties of the lattice displacement perpendicular to the bond direction. As an example, we also depict θ_2 that is the angle of bond-2 orientation and the x direction.

distance a, for atom 1 we thus have three nearest neighbors at

$$\begin{aligned}\boldsymbol{\delta}_1^{(0)} &= a(1,0),\\ \boldsymbol{\delta}_2^{(0)} &= a(-1/2,\sqrt{3}/2),\\ \boldsymbol{\delta}_3^{(0)} &= a(-1/2,-\sqrt{3}/2).\end{aligned} \tag{6}$$

Such geometrical structure is reflected in a corresponding Brillouin zone as shown in Fig. 2(b). To investigate the features of the lattice dynamics and the lattice eigenmodes analytically, we employ a force-constant model where the elastic properties are determined by a set of spring parameters associated with each interatomic bond. We define the vector of the lattice displacements for the unit cell i in real $\mathbf{u}_i$ and momentum $\mathbf{u}_\mathbf{q}$ spaces as follows:

$$\mathbf{u}_i = \begin{bmatrix} u_{1,x}(\mathbf{r}_i)\\ u_{1,y}(\mathbf{r}_i)\\ u_{2,x}(\mathbf{r}_i)\\ u_{2,y}(\mathbf{r}_i)\end{bmatrix}, \quad \mathbf{u}_\mathbf{q} = \begin{bmatrix} u_{1,x}(\mathbf{q})\\ u_{1,y}(\mathbf{q})\\ u_{2,x}(\mathbf{q})\\ u_{2,y}(\mathbf{q})\end{bmatrix}. \tag{7}$$

The equation of motion for the lattice displacement along each direction and for each atom reads

$$\hat{\mathbf{M}}\cdot\left(\frac{\partial^2\mathbf{u}_i}{\partial t^2}\right) = -\sum_{\langle j\rangle_i}\hat{\mathbf{K}}_{i-j}\cdot\mathbf{u}_j, \tag{8}$$

where $\hat{\mathbf{M}}$ is the diagonal mass matrix,

$$\hat{\mathbf{M}} = \begin{bmatrix} M_1 & 0 & 0 & 0\\ 0 & M_1 & 0 & 0\\ 0 & 0 & M_2 & 0\\ 0 & 0 & 0 & M_2\end{bmatrix}, \tag{9}$$

and $\hat{\mathbf{K}}_{i-j}$ is the matrix of the elastic constants in the real space. Equation (8) can be equivalently written in the momentum space:

$$\hat{\mathbf{M}}\cdot\left(\frac{\partial^2\mathbf{u}_\mathbf{q}}{\partial t^2}\right) = -\hat{\mathbf{K}}_\mathbf{q}\cdot\mathbf{u}_\mathbf{q}. \tag{10}$$

For practical purposes, it is more convenient to introduce the dynamical matrix $\hat{\mathbf{D}}_\mathbf{q}$, based on the Löwdin's orthogonalization [36], defined as

$$\hat{\mathbf{D}}_\mathbf{q} = \hat{\mathbf{M}}^{-1/2}\cdot\hat{\mathbf{K}}_\mathbf{q}\cdot\hat{\mathbf{M}}^{-1/2}, \tag{11}$$

and in the frequency space we get the (diagonal) matrix of the phonon dispersion $\boldsymbol{\omega}_\mathbf{q}$ (and the corresponding eigenvectors) from the solution:

$$\hat{\mathbf{D}}_\mathbf{q}\cdot\boldsymbol{\epsilon}_{\mathbf{q},\lambda} = \boldsymbol{\omega}^2_{\mathbf{q},\lambda}\cdot\boldsymbol{\epsilon}_{\mathbf{q},\lambda}. \tag{12}$$

Here the index λ denotes the different branches of the phonon dispersion.

The matrix $\hat{\mathbf{K}}_{i-j}$ can be evaluated at different degrees of approximation, including a large number of force-constant parameters to reproduce the realistic phonon dispersion of specific materials [37–39]. For the purpose of the present paper, however, to highlight the relevant physics governing the chiral phonon properties, and following Ref. [20], we employ a minimal model containing only one radial (ϕ_r) and one transverse (ϕ_t) force constant acting between nearest-neighbor atoms [see Fig. 2(c)]. It is convenient to define in the Cartesian $x-y$ space the stiffness matrix along with bond 1 as

$$\boldsymbol{\Phi}_1 = \begin{bmatrix}\phi_r & 0\\ 0 & \phi_t\end{bmatrix}. \tag{13}$$

In a similar way, the stiffness matrix operative for bonds 2 and 3 can be obtained just with a rotation matrix by $\pm\theta = \pm 2\pi/3$, namely,

$$\begin{aligned}\boldsymbol{\Phi}_2 &= \mathbf{U}^{-1}(\theta)\boldsymbol{\Phi}_1\mathbf{U}(\theta) = \frac{1}{4}\begin{bmatrix}\phi_r+3\phi_t & -\sqrt{3}(\phi_r-\phi_t)\\ -\sqrt{3}(\phi_r-\phi_t) & 3\phi_r+\phi_t\end{bmatrix},\\ \boldsymbol{\Phi}_3 &= \mathbf{U}^{-1}(-\theta)\boldsymbol{\Phi}_1\mathbf{U}(-\theta) = \frac{1}{4}\begin{bmatrix}\phi_r+3\phi_t & \sqrt{3}(\phi_r-\phi_t)\\ \sqrt{3}(\phi_r-\phi_t) & 3\phi_r+\phi_t\end{bmatrix},\end{aligned} \tag{14}$$

For the unstrain case, we have $\theta = 2\pi/3$ and therefore the unitary transformation $\mathbf{U}(\theta)$ reads

$$\mathbf{U}(\theta) = \begin{bmatrix}\cos\theta & \sin\theta\\ -\sin\theta & \cos\theta\end{bmatrix} = \begin{bmatrix}-1/2 & \sqrt{3}/2\\ -\sqrt{3}/2 & -1/2\end{bmatrix}. \tag{15}$$

With the help of Eqs. (13) and (14), we can finally get an analytical expression for $\hat{\mathbf{K}}_\mathbf{q}$:

$$\hat{\mathbf{K}}_\mathbf{q} = \sum_{i=1}^{3}\begin{bmatrix}\boldsymbol{\Phi}_i & -\boldsymbol{\Phi}_i e^{i\mathbf{q}\cdot\boldsymbol{\delta}_i^{(0)}}\\ -\boldsymbol{\Phi}_i e^{-i\mathbf{q}\cdot\boldsymbol{\delta}_i^{(0)}} & \boldsymbol{\Phi}_i\end{bmatrix}. \tag{16}$$

B. Anisotropic strain

In the presence of anisotropic strain, the stiffness matrices in Eqs. (13) and (14) need to be adjusted to account for *two* different effects: (i) the geometrical change of the angles between neighbor atoms, implying different mixing of the x and y components of the lattice displacements; and (ii) the elongation/compression of the bonds, tuning the spring constants $\phi_r(R)$, $\phi_t(R)$ whose values depend intrinsically on the interatomic distance R, in a similar way as the case of hopping energies in electronic tight-binding models [8,40–45]. Both effects descend from the strain-induced change in the nearest-neighbor vectors, which are modified as

$$\boldsymbol{\delta}_i = (1+\boldsymbol{\varepsilon})\cdot\boldsymbol{\delta}_i^{(0)}. \tag{17}$$

Therefore, we find

$$\begin{aligned}\boldsymbol{\delta}_1 &= a(1+\varepsilon_{xx},\varepsilon_{xy}),\\ \boldsymbol{\delta}_2 &= \frac{a}{2}(-1-\varepsilon_{xx}+\sqrt{3}\varepsilon_{xy},\sqrt{3}(1+\varepsilon_{yy})-\varepsilon_{xy}),\\ \boldsymbol{\delta}_3 &= \frac{a}{2}(-1-\varepsilon_{xx}-\sqrt{3}\varepsilon_{xy},-\sqrt{3}(1+\varepsilon_{yy})-\varepsilon_{xy}).\end{aligned} \tag{18}$$

Focusing first on the geometrical effect, it is useful to define the modified angle in the Cartesian space between the two bond atoms according to the relation

$$\tan\theta_i = \delta_{i,y}/\delta_{i,x}. \tag{19}$$

The rotation matrix for each bond is thus generalized as

$$\mathbf{U}(\theta_i) = \begin{bmatrix}\cos\theta_i & \sin\theta_i\\ -\sin\theta_i & \cos\theta_i\end{bmatrix}, \tag{20}$$

resulting in the following expressions along each bond in the strained system:

$$\mathbf{U}(\theta_1) = \begin{bmatrix} 1 & \varepsilon_{xy} \\ -\varepsilon_{xy} & 1 \end{bmatrix},$$
$$\mathbf{U}(\theta_2) = \frac{1}{8}\begin{bmatrix} -3\varepsilon_{yy} + 2\sqrt{3}\varepsilon_{xy} + 3\varepsilon_{yy} - 4 & -\sqrt{3}\varepsilon_{xx} + 2\varepsilon_{xy} + \sqrt{3}(\varepsilon_{yy} + 4) \\ \sqrt{3}\varepsilon_{xx} - 2\varepsilon_{xy} - \sqrt{3}(\varepsilon_{yy} + 4) & -3\varepsilon_{xx} + 2\sqrt{3}\varepsilon_{xy} + 3\varepsilon_{xy} - 4 \end{bmatrix},$$
$$\mathbf{U}(\theta_3) = \frac{1}{8}\begin{bmatrix} -3\varepsilon_{xy} - 2\sqrt{3}\varepsilon_{xy} + 3\varepsilon_{yy} - 4 & \sqrt{3}\varepsilon_{xx} + 2\varepsilon_{xy} - \sqrt{3}(\varepsilon_{yy} + 4) \\ -\sqrt{3}\varepsilon_{xx} - 2\varepsilon_{xy} + \sqrt{3}(\varepsilon_{yy} + 4) & -3\varepsilon_{yy} - 2\sqrt{3}\varepsilon_{xx} + 3\varepsilon_{yy} - 4 \end{bmatrix}. \quad (21)$$

Note that such a geometrical effect is not present in the case of biaxial strain that preserves the perfect hexagonal symmetry.

As mentioned, besides the pure geometrical change is the stiffness matrix induced by the change in the angles between neighbor atoms, one should account for the strain-induced change in the value of the spring constants $\phi_r(R)$, $\phi_t(R)$. As explicited in the expression, the strength of such parameters depends itself on the interatomic distance R and in the presence of strain is also changed according to the expression

$$\phi^{\varepsilon}_{i,\ell} = \phi_\ell\left[1 - \frac{\beta_\ell}{a^2}\boldsymbol{\delta}^{(0)}_i \cdot \boldsymbol{\varepsilon} \cdot \boldsymbol{\delta}^{(0)}_i\right], \quad (22)$$

where $\beta_{\ell=r,t} = -\partial \ln \phi_\ell / \partial \ln(a)$. Once both geometrical and energy effects are taken into account, we thus obtain the complete relations:

$$\hat{\boldsymbol{\Phi}}^{\varepsilon}_1 = \begin{bmatrix} \phi^{\varepsilon}_{1,r} & g_1(\phi^{\varepsilon}_{1,r} - \phi^{\varepsilon}_{1,t}) \\ g_1(\phi^{\varepsilon}_{1,r} - \phi^{\varepsilon}_{1,t}) & \phi^{\varepsilon}_{1,t} \end{bmatrix},$$
$$\hat{\boldsymbol{\Phi}}^{\varepsilon}_2 = \begin{bmatrix} \phi^{\varepsilon}_{2,r}g_2 + \phi^{\varepsilon}_{2,t}g_3 & -(\phi^{\varepsilon}_{2,r} - \phi^{\varepsilon}_{2,t})g_4 \\ -(\phi^{\varepsilon}_{2,r} - \phi^{\varepsilon}_{2,t})g_4 & \phi^{\varepsilon}_{2,t}g_2 + \phi^{\varepsilon}_{2,r}g_3 \end{bmatrix},$$
$$\hat{\boldsymbol{\Phi}}^{\varepsilon}_3 = \begin{bmatrix} \phi^{\varepsilon}_{3,r}g_2 + \phi^{\varepsilon}_{3,t}g_3 & (\phi^{\varepsilon}_{3,r} - \phi^{\varepsilon}_{3,t})g_4 \\ (\phi^{\varepsilon}_{3,r} - \phi^{\varepsilon}_{3,t})g_4 & \phi^{\varepsilon}_{3,t}g_2 + \phi^{\varepsilon}_{3,r}g_3 \end{bmatrix}. \quad (23)$$

The elastic constants along each bond in the strained lattice are given by

$$\phi^{\varepsilon}_{1,\ell} = \phi_\ell\{1 - \beta_\ell\varepsilon_{xx}\},$$
$$\phi^{\varepsilon}_{2,\ell} = \phi_\ell\{1 - \beta_\ell\frac{1}{4}(\varepsilon_{xx} - 2\sqrt{3}\varepsilon_{xy} + 3\varepsilon_{yy})\},$$
$$\phi^{\varepsilon}_{3,\ell} = \phi_\ell\{1 - \beta_\ell\frac{1}{4}(\varepsilon_{xx} + 2\sqrt{3}\varepsilon_{xy} + 3\varepsilon_{yy})\}, \quad (24)$$

where

$$g_1 = \varepsilon_{xy},$$
$$g_2 = \frac{2 + 3(\varepsilon_{xx} - \varepsilon_{yy}) - 2\sqrt{3}\varepsilon_{xy}}{8},$$
$$g_3 = \frac{6 - 3(\varepsilon_{xx} - \varepsilon_{yy}) + 2\sqrt{3}\varepsilon_{xy}}{8},$$
$$g_4 = \frac{2\sqrt{3} + \sqrt{3}(\varepsilon_{xx} - \varepsilon_{yy}) - 2\varepsilon_{xy}}{8}. \quad (25)$$

Equations (23) and (24), once plugged in Eq. (16), define the matrix of the elastic constants $\hat{\mathbf{K}}_{\mathbf{q}}$, and hence the dynamical matrix $\hat{\mathbf{D}}_{\mathbf{q}}$, in the presence of strain, taking into account both the geometrical effects and the changes in the spring strengths.

IV. STRAIN-DRIVEN CHIRAL PHONON MODES

Equipped with the above theoretical modeling of the lattice dynamics in the presence of strain, we can now investigate how uniaxial strain can give rise to chiral modes with specific controlled momentum.

The fundamental information will be obtained from Eq. (12), where the eigenvalues of the dynamical matrix provide the phonon dispersion $\omega_\lambda(\mathbf{q})$ whereas the eigenvectors $\boldsymbol{\epsilon}_\lambda(\mathbf{q})$ rule the lattice displacements and carry the information about the chiral character. This can be captured by switching the representation of the lattice displacements from the Cartesian basis $|x_1\rangle$, $|y_1\rangle$, $|x_2\rangle$, $|y_2\rangle$, to the chiral basis defined by $|R_\alpha\rangle = (|x_\alpha\rangle + i|y_\alpha\rangle)/\sqrt{2}$, $|L_\alpha\rangle = (|x_\alpha\rangle - i|y_\alpha\rangle)/\sqrt{2}$, $(\alpha = 1, 2)$. It is thus convenient to introduce the phonon circular polarization [20],

$$s_{z,\lambda}(\mathbf{q}) = \sum_{\alpha=1,2}(|\epsilon_{R,\alpha,\lambda}(\mathbf{q})|^2 - |\epsilon_{L,\alpha,\lambda}(\mathbf{q})|^2), \quad (26)$$

where $\epsilon_{R/L,\alpha,\lambda}$ are the phonon eigenvectors of the dynamical matrix expressed in the chiral basis. The phonon circular polarization is strictly related to the phonon orbital angular momentum, which can be defined for each phonon band as

$$L_{z,\lambda}(\mathbf{q}) = \hbar s_{z,\lambda}(\mathbf{q})\{n_{\mathrm{B}}(\omega_\lambda(\mathbf{q})/T) + 1/2\}, \quad (27)$$

where $n_{\mathrm{B}}(x) = 1/[\exp(x) - 1]$ is the Bose-Einstein factor. In the following, to better show the results of our paper, we use the same force constant parameters employed in Ref. [20], $\phi_r = 1$, $\phi_t = 0.25$, with an atomic mass difference $M_1 = 1$, $M_2 = 3$ that reproduces qualitatively the case of MoS_2. We also take the value of the parameters β_l appearing in Eq. (22) as $\beta_{l=r,t} = 3$, which is a reasonable estimate in many materials. In the absence of strain, the phonon dispersion displays four bands (we number them $\lambda = 1, \ldots, 4$, from lower to higher energies) with two optical branches degenerate at Γ with E_{2g} symmetry and two acoustic branches. In agreement with Ref. [20], for the perfect hexagonal lattice, we find chiral modes with an opposite chirality at the K, K′ points for bands 2 and 3. An inspection of the eigenvectors shows that such chiral modes have a pure-sublattice character, with the mode of band 2 (3) involving chiral lattice displacements only of the heavier (lighter) sublattice.

To reveal more clearly the onset of unique chiral modes upon the application of an anisotropic strain, we consider a strain tensor corresponding to a pure uniaxial tensile uniaxial tensile strain $\varepsilon_+ = 2\%$ $(\varepsilon_- = 0)$ along the x (armchair)

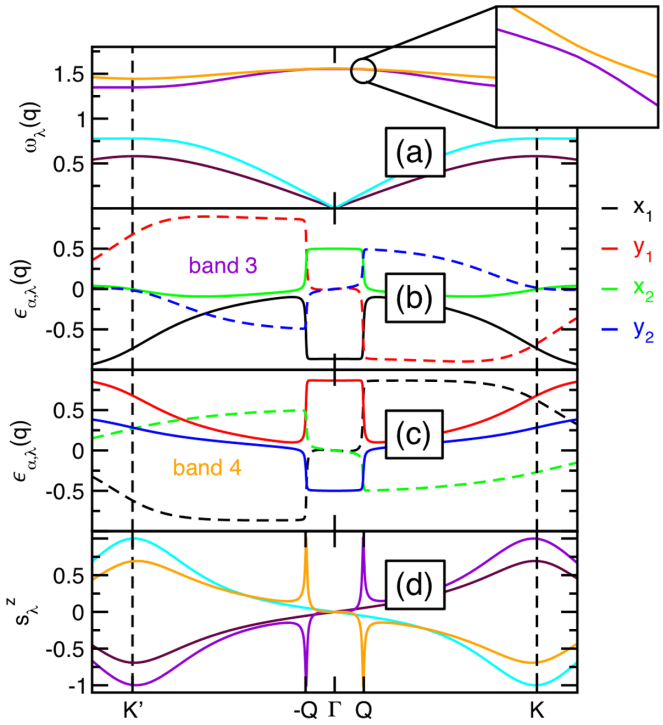

FIG. 3. (a) Phonon dispersion along the cut K′ − Γ-K for the force-constant model described in the text, upon a uniaxial tensile strain $\varepsilon_+ = 2\%$ along the x direction. Brown, cyan, violet, and orange lines denote phonon bands from $\lambda = 1, \ldots, 4$, respectively. Inset: A magnification of the region close to the avoided-band-crossing point Q. (b), (c) Corresponding eigenvectors of the lattice displacements of bands 3 and 4. Black, red, green, and blue lines show the normalized lattice displacement along x_i and y_i for atom i. Solid lines represent the real component, whereas dashed lines denote the imaginary part. (d) Corresponding phonon circular polarization $s_{z,\lambda}$ for all four bands. Color code as in (a).

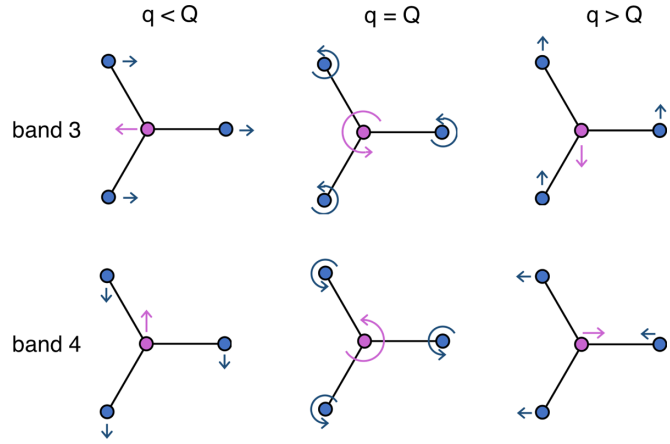

FIG. 4. Sketch of the evolution of the relevant lattice displacement fields close to the avoided band crossing, giving rise to unique chiral modes. A uniaxial tensile strain along the x axis is assumed. The top panel corresponds to the upper optical phonon band 4, lower panel to the lower optical phonon band 3. For $q_y < Q$, the lattice displacements are dictated by the strain direction, as for the Γ point, with the softer mode being aligned to the tensile strain and the harder mode in the orthogonal direction. Due to the band inversion, the opposite scenario occurs for $q_y > Q$. At $q_y = Q$, the hybridization with complex coefficients of the two modes gives rise to chiral lattice displacement fields, with opposite chirality in the two phonon branches.

direction ($\theta_+ = 0$). The corresponding phonon dispersion along the relevant vertical cut K′ − Γ-K is shown in Fig. 3(a). At the Γ point ($\mathbf{q} = 0$), we observe the well-known splitting (very tiny on this scale) of the E_{2g} phonons in two nondegenerate modes $\omega_-(\Gamma)$, $\omega_+(\Gamma)(\omega_-(\Gamma) < \omega_+(\Gamma))$ with eigenvectors aligned along θ_+, θ_-, respectively. As a general rule, the softer mode ω_- corresponds to lattice displacements along the tensile axis θ_+ of strain direction (in this case, the x direction), while the harder mode ω_+ is associated with the compressive strain along θ_-. Such splitting, for the tensile strain along x, implies a band crossing at momenta $\pm Q$ along with the y-axis K′ − Γ-K cut based on the simple model here considered with transverse-optical (TO) modes harder than the longitudinal-optical (LO) ones. For the simple model here considered, the TO mode is harder than the LO mode, unlike the predictions of fully *ab initio* calculations. This discrepancy does not affect the validity of the results of our analysis, with the simple warning that predictions for tensile strain might apply to compressive strain and vice versa. A closer look at the phonon dispersion [see inset of Fig. 3(a)] reveals that such phonon-band-crossing is just apparent but is actually an avoided-band-crossing with a finite gap $\Delta\omega_{\rm chi} = \omega_+(Q) - \omega_-(Q)$ between the two phonon branches.

A deeper understanding of the physics here at work can be attained from the analysis of the phonon mode eigenvectors $\epsilon_{\alpha,\lambda}(\mathbf{q})$ [Figs. 3(b) and 3(c)]. As expected, close to the Γ point, in the strained case, band 3 and band 4 are characterized by lattice displacements almost purely aligned along x and y, respectively, with atom 2 moving counterphase versus atom 1 (see Fig. 4). The opposite occurs for momenta larger than the crossing point, where the order of the bands is reversed. A true band crossing would happen if the eigenvectors were purely real. However, a small imaginary component is always unavoidably present at finite momenta. The presence of such a finite imaginary part prevents a true crossing expected between bands with orthogonal lattice displacements, and the switch between the lattice displacements of band 3 for $|q_y| \leqslant Q$ and band 4 for $|q_y| \geqslant Q$ occurs through a sudden *chiral twist* where the real x component acquires an imaginary y component and vice versa (middle panels in Fig. 4). An analytical description is provided in Sec. V. Right at the momentum of the avoided-crossing point, $q_y = \pm Q$, the eigenmodes of bands 3 and 4 are described exactly by the chiral basis. This is remarkably evident in the phonon circular polarization $s_{z,\lambda}(\mathbf{q})$ for each band shown in Fig. 3(d). Here we can clearly see that, besides the well-known chiral phonons at K, K′, *unique* chiral phonons appear upon anisotropic strain in bands 3 and 4 close to the Γ point, with opposite circular phonon polarization at $\pm Q$. It is worth stressing that such chiral phonons present strikingly different properties with respect to the standard chiral phonon pointed out in Refs. [20,22]. Indeed, while chiral phonons discussed in Refs. [20,22] are locked at the high-symmetry points K, K′ at the edge of the Brillouin zone, and they obey a threefold symmetry, the chiral phonons arising

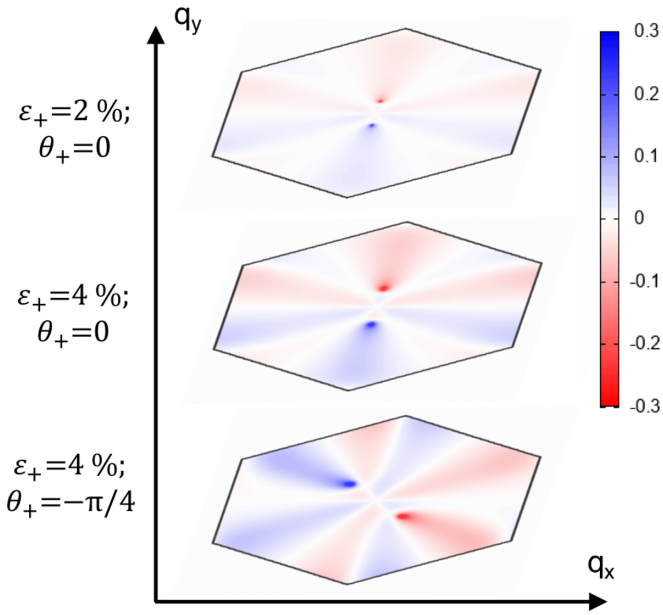

FIG. 5. Color map of $\Delta s_{z,\lambda}$ for the optical phonon band 4 upon different values and directions of applied strain. Red and blue regions represent positive and negative phonon circular polarizations, respectively.

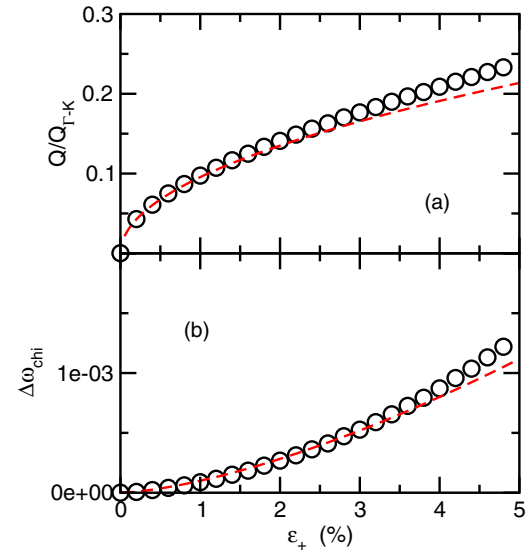

FIG. 6. Dependence of crossing point **Q** (a) and of the phonon gap $\Delta\omega_{\rm chi}$ (b) upon the strain magnitude for uniaxial tensile strain along the x direction ($\theta_+ = 0$). Black symbols represent results using the full force-constant model; the dashed red line the analytical predictions using the two-band model.

upon anisotropic strain have a *tunable* location in the Brillouin zone controlled by the strength and by the direction of the strain. Since for vanishing strain $|\varepsilon| \to 0$ the **q** momentum of such chiral phonon approaches zero, $|\mathbf{Q}| \to 0$, for small strain, these phonons are expected to appear close to the Γ point, where spectroscopic optical probes can be effective.

To highlight the role of the anisotropic strain, we analyze for each phonon band the change in the phonon's circular polarization induced by the anisotropic strain, namely, $\Delta s_{z,\lambda} = s_{z,\lambda}(\hat{\varepsilon}) - s_{z,\lambda}(\hat{\varepsilon} = 0)$. The tunability of such chiral phonons by means of strain is shown in Fig. 5 where we plot in a color map $\Delta s_{z,\lambda}$ of the optical phonon band $\lambda = 4$ for different magnitudes and directions of the applied strain. We see that increasing strain shifts the momentum $\pm\mathbf{Q}$ of chiral phonons at larger values, whereas the presence of a shear component rotates **Q** away from the crystallographic axes. As a general rule, a couple of such strain-induced chiral phonons with opposite circular polarization appears along the direction in the reciprocal space *perpendicular* to the strain tensile component in real space.

The dependence of **Q** on the strain magnitude is shown in Fig. 6(a), while in Fig. 6(b) we plot the value of the phonon gap $\Delta\omega_{\rm chi}$ between bands 4 and 3. The numerical results appear consistent with a square-root behavior for the momentum $Q \sim \sqrt{\Delta\varepsilon}$, whereas the gap shows a dependence $\Delta\omega_{\rm chi} \sim (\Delta\varepsilon)^{3/2}$.

V. LOW-ENERGY MODEL DESCRIPTION

Complete control and prediction of the properties of these chiral phonons upon strain can be analytically achieved by introducing an effective reduced-model based on a Schrieffer-Wolf transformation.

For practical purposes, we perform the derivation in the Cartesian space, whereas the equivalent expression in the chiral basis can be eventually obtained by a final rotation. We start our analysis by defining the dynamical matrix of the full lattice model at the Γ point ($\mathbf{q} = \mathbf{0}$):

$$\hat{\mathbf{D}}_\Gamma = \sum_{i=1}^{3} \begin{bmatrix} \hat{\mathbf{\Phi}}_i/M_1 & -\hat{\mathbf{\Phi}}_i/\sqrt{M_1 M_2} \\ -\hat{\mathbf{\Phi}}_i/\sqrt{M_1 M_2} & \hat{\mathbf{\Phi}}_i/M_2 \end{bmatrix}. \tag{28}$$

Such matrix can be diagonalized by the unitary transformation $\hat{\mathbf{\Lambda}}_\Gamma$: $\hat{\mathbf{D}}'_\Gamma = \hat{\mathbf{\Lambda}}_\Gamma \hat{\mathbf{D}}_\Gamma \hat{\mathbf{\Lambda}}_\Gamma^{-1}$. It is straightforward to notice that

$$\hat{\mathbf{D}}'_\Gamma = \omega_\Gamma^2 \begin{bmatrix} \hat{\mathrm{I}}_{2\times 2} & \hat{0}_{2\times 2} \\ \hat{0}_{2\times 2} & \hat{0}_{2\times 2} \end{bmatrix}, \tag{29}$$

where $\hat{\mathrm{I}}_{2\times 2}$, $\hat{0}_{2\times 2}$ are the identity matrix and the null matrix, respectively, in the 2×2 space. The unitary transformation $\hat{\mathbf{\Lambda}}_\Gamma$ can now be used to express in such basis the full lattice dynamical matrix for generic **q**: $\hat{\mathbf{D}}'_\mathbf{q} = \hat{\mathbf{\Lambda}}_\Gamma \hat{\mathbf{D}}_\mathbf{q} \hat{\mathbf{\Lambda}}_\Gamma^{-1}$. In full generality, $\hat{\mathbf{D}}'_\mathbf{q}$ can be decomposed as

$$\hat{\mathbf{D}}'_\mathbf{q} = \hat{\mathbf{D}}'_{0,\mathbf{q}} + \hat{\mathbf{V}}_\mathbf{q}, \tag{30}$$

where $\hat{\mathbf{D}}'_{0,\mathbf{q}}$ is block diagonal with respect to the subspaces of optical and acoustic modes whereas $\hat{\mathbf{V}}_\mathbf{q}$ is off-diagonal and it accounts for the finite hybridization between these two blocks:

$$\hat{\mathbf{D}}'_{0,\mathbf{q}} = \begin{bmatrix} \hat{\mathbf{D}}'_{\mathrm{d,op}} & 0 \\ 0 & \hat{\mathbf{D}}'_{\mathbf{q},\mathrm{ac}} \end{bmatrix}, \quad \hat{\mathbf{V}}_\mathbf{q} = \begin{bmatrix} 0 & \hat{\mathbf{V}}_{\mathbf{q},\mathrm{op-ac}} \\ \hat{\mathbf{V}}^\dagger_{\mathbf{q},\mathrm{op-ac}} & 0 \end{bmatrix}. \tag{31}$$

By construction, it is easy to see that $\hat{\mathbf{V}}_\mathbf{q} \to 0$ for $|\mathbf{q}| \to 0$. To obtain an effective model valid at the q^2 order for the two-band subset of the optical modes, we expand the matrix elements $\hat{\mathbf{D}}'_{0,\mathbf{q}}$ up to the q^2 order and $\hat{\mathbf{V}}_\mathbf{q}$ up to the linear order. The final

effective model is thus achieved by performing the Schrieffer-Wolf transformation,

$$\hat{\mathbf{D}}''_{\mathbf{q}} = e^{-\hat{\mathcal{S}}_{\mathbf{q}}}, \hat{\mathbf{D}}'_{\mathbf{q}} e^{\hat{\mathcal{S}}_{\mathbf{q}}}, \approx \hat{\mathbf{D}}'_{\mathbf{q}} + \hat{\mathbf{V}}_{\mathbf{q}} + [\hat{\mathbf{D}}'_{\mathbf{q}}, \hat{\mathcal{S}}_{\mathbf{q}}] + [\hat{\mathbf{V}}_{\mathbf{q}}, \hat{\mathcal{S}}_{\mathbf{q}}] + \frac{1}{2}[[\hat{\mathbf{D}}'_{\mathbf{q}}, \hat{\mathcal{S}}_{\mathbf{q}}], \hat{\mathcal{S}}_{\mathbf{q}}] + \text{higher-order terms}, \tag{32}$$

where $\hat{\mathcal{S}}_{\mathbf{q}}$ has an off-diagonal form

$$\hat{\mathcal{S}}_{\mathbf{q}} = \begin{bmatrix} \hat{0}_{2\times 2} & \hat{\eta}_{\mathbf{q}} \\ -\hat{\eta}^{\dagger}_{\mathbf{q}} & \hat{0}_{2\times 2} \end{bmatrix}, \tag{33}$$

and where the 2×2 matrix $\hat{\eta}_{\mathbf{q}}$ can be identified by imposing the condition of cancellation of off-diagonal (the q-linear) terms:

$$\hat{\mathbf{V}}_{\mathbf{q}} + [\hat{\mathbf{D}}'_{\mathbf{q}}, \hat{\mathcal{S}}_{\mathbf{q}}] = 0. \tag{34}$$

The final effective model in the 2×2 subset of optical branches follows

$$\hat{\mathbf{D}}''_{\text{eff,op}} = \hat{\mathbf{D}}'_{\text{d,op}} + \frac{1}{2}[\hat{\eta}^{\dagger}_{\mathbf{q}} \hat{\mathbf{V}}_{\mathbf{q},\text{op-ac}} + \hat{\mathbf{V}}^{\dagger}_{\mathbf{q},\text{op-ac}} \hat{\eta}_{\mathbf{q}}]. \tag{35}$$

The 2×2 model so obtained is derived in the Cartesian Hilbert space. It is, however, more convenient to work directly in the chiral basis, $v_L = (v_3 + iv_4)/\sqrt{2}$, $v_R = (v_3 - iv_4)/\sqrt{2}$. In such a chiral basis, the phonon properties are described by the dynamical matrix up to the linear order in strain,

$$\hat{D}_0(\mathbf{q}) + D_{\varepsilon}(\mathbf{q}), \tag{36}$$

where $\hat{D}_0(\mathbf{q})$ accounts for the lattice properties in the absence of strain, while $D_{\varepsilon}(\mathbf{q})$ contains the corrections due to an anisotropic strain. More explicitly, close to the Γ point, we can write

$$\hat{D}_0(\mathbf{q}) = \omega_{\Gamma}^2 \begin{bmatrix} 1 - a_0|\mathbf{q}|^2 & a_1 q_L^2 \\ a_1 q_R^2 & 1 - a_0|\mathbf{q}|^2 \end{bmatrix}, \tag{37}$$

where $q_{L/R} = q_x \pm iq_y$. The resulting phonon bands in unstrained case are thus described by

$$\omega_{\pm}(\mathbf{q}) = \gamma_{\pm}(\mathbf{q})\omega_{\Gamma}, \tag{38}$$

where

$$\gamma_{\pm}^2(\mathbf{q}) = 1 - (a_0 \pm a_1)|\mathbf{q}|^2. \tag{39}$$

The strain correction term, on the other hand, can be computed at the leading order in the $\mathbf{q} \to 0$ limit and it reads

$$\hat{D}_{\varepsilon}(\mathbf{q} = 0) = \omega_{\Gamma}^2 \begin{bmatrix} -2\alpha_0 \varepsilon_0 & \alpha_1 \varepsilon_R \\ \alpha_1 \varepsilon_L & -2\alpha_0 \varepsilon_0 \end{bmatrix}, \tag{40}$$

where $\varepsilon_{L/R} = \varepsilon_{xx} - \varepsilon_{yy} \pm i2\varepsilon_{xy}$. The phonon bands *in the presence of anisotropic strain*, computed by diagonalizing $\hat{D}_0(\mathbf{q}) + D_{\varepsilon}(0)$, thus read

$$\omega_{\pm}(\mathbf{q}) = \gamma_{\pm,\varepsilon}(\mathbf{q})\omega_{\Gamma}, \tag{41}$$

where

$$\gamma_{\pm,\varepsilon}^2(\mathbf{q}) = 1 - a_0|\mathbf{q}|^2 - 2\alpha_0\varepsilon_0 \pm \sqrt{\left[a_1(q_x^2 - q_y^2) - \alpha_1\left(\varepsilon_{xx} - \varepsilon_{yy}\right)\right]^2 + 4[a_1 q_x q_y + \alpha_1 \varepsilon_{xy}]^2}. \tag{42}$$

The numerical values of a_0, a_1 are dictated by the microscopical parameters of the force-constant model. Using the values employed in the main text, $\phi_r = 1$, $\phi_t = 0.25$, $M_1 = 1$, $M_2 = 3$, we obtain numerically $a_0 = 123/1600$, $a_1 = 9/320$, $\alpha_0 = 3/2$, and $\alpha_1 = 3/20$. Note that, although the parameters a_i, α_i are here evaluated within the minimal nearest-neighbor force-constant model, the validity of Eqs. (37)–(42) holds true in full generality for realistic phonon bands where the parameters a_i, α_i, as discussed later, can be extracted from first-principles calculations or from direct experimental probes. Based on Eq. (42), we can now analytically identify, limited to a quadratic expansion in $\mathbf{q}^2$, the momentum Q where a band anticrossing occurs and chiral phonons appear. For the instructive example of uniaxial tensile strain along the x direction, $\varepsilon_+ \neq 0$, $\varepsilon_- = 0$, $\theta_+ = 0$, we find $\mathbf{Q} = (0, Q_y)$, where

$$Q_y = \pm\sqrt{\frac{\alpha_1 \varepsilon_+}{a_1}}. \tag{43}$$

Using the values of $a_0, a_1, \alpha_0, \alpha_1$ derived above, we obtain the analytical predictions shown in Fig. 6, in perfect agreement with the numerical results for the full phonon band dispersion [Fig. 3(a)]. For generic case, including shear strain, we find that the momentum $\mathbf{Q}_{\pm} = \pm Q(\cos\phi, \sin\phi)$ is univocally determined by the strain tensor, with the angle ϕ aligned along the compression direction, $\phi = \theta_-$, and Q^2 being determined by the strain difference between the two main components:

$$Q^2 = \left|\frac{\alpha_1}{a_1}\right| \Delta\varepsilon. \tag{44}$$

It is worth mentioning that using in Eqs. (37)–(40) an expansion for small strains hence small $\mathbf{q}'$s is very efficient in determining the location of these chiral modes and predicting a *true* phonon band crossing with two degenerate modes at $\mathbf{Q}$, not a well-defined chiral character. A true gap, and thus a robust chiral character, is recovered, however, in a more realistic modeling when a higher-order dependence on the momenta is retained. From a dimensional analysis, since $|Q|$ scales with the square root of the strain amplitude, one can realize that the next leading order effects are driven by the cubic $\mathbf{q}^3$ terms in Eq. (37), which lead to a correction $\hat{D}_0(\mathbf{q}) \to \hat{D}_0(\mathbf{q}) + \hat{D}_1(\mathbf{q})$, where $\hat{D}_1(\mathbf{q}) \propto A|\mathbf{q}|^3\hat{\sigma}_3$. The gap $\Delta\omega_{\text{chi}} = \omega_+(\mathbf{Q}) - \omega_-(\mathbf{Q})$ between the two unique chiral modes appearing under strain is predicted thus to behave as

$$\Delta\omega_{\text{chi}} \propto (\Delta\varepsilon)^{3/2} \sin(3\phi). \tag{45}$$

The strain dependence of the gap $\Delta\omega_{\text{chi}}$ between the two chiral modes is also shown in Fig. 6(b) by comparing the numerical results obtained by the effective phonon dispersion evaluated with the force-constant model with the effective two-band model. Once again, we find a striking agreement.

VI. DISCUSSION AND EXPERIMENTAL PROBES

In the above sections, we have elucidated the fundamental physical mechanisms ruling the onset of unique chiral modes in the presence of anisotropic strain. To this aim, we have employed the simplest minimal model containing all the basic physics needed to account for this phenomenon. To assess the actual role of these modes in physical observables, and to

outline possible experimental probes, a further step toward a more quantitative analysis is needed based on material details.

Hexagonal boron-nitride (h-BN) and TMDs are among the best candidates for detecting and manipulating chiral phonons. Focusing on the in-plane optical branches close to the Γ point, typical phonon energy scales range from $\omega(\Gamma) \approx 1350 - 1370$ cm^{-1} for monolayer h-BN [39,46–48] to $\omega(\Gamma) \approx 385 - 390/357/248$ cm^{-1} in monolayer $MoS_2/WS_2/WSe_2$, respectively [49,50]. Using Fig. 6 as a qualitative estimate, and considering realistic values of the strain, the gap predicted by such simple modeling can be of the order of a fraction or 1 cm^{-1}.

It should be kept in mind, however, that the simple model so far employed is just meant to point out the fundamental mechanisms, but that for quantitative analysis in real systems, one should take into account detailed material characteristics. However, the predicted strain-induced band inversion of two optical bands is a robust feature independent of the material characteristics.

Focusing on the case of h-BN as a template, we take a proper mass choice $M_1 = 10.8$, $M_2 = 14$ a.m.u., and we can estimate $\phi_r = 166$ eV/Å^2, $\phi_t = 83$ eV/Å^2, corresponding, in the unstrained case, to an optical in-plane phonon frequency $\omega_{3/4}(\Gamma) = 1370$ cm^{-1} and to a phonon frequency of the highest optical branch at the K point $\omega_4(\mathrm{K}) = 1120$ cm^{-1}, in agreement with first-principles calculations [48]. With these values, and assuming $\beta_l = 3$, for an uniaxial strain of 2% along the x direction, we get a strain-driven splitting of the optical modes at the Γ point as $\delta\omega_{\pm}(\Gamma) \approx 3$ cm^{-1} and the onset of chiral phonons at $|\mathbf{Q}| = 0.2$ Å^{-1}, with a gap between the chiral modes $\Delta\omega_{\mathrm{chi}} \approx 0.2$ cm^{-1}. These model-based estimates can be compared with an analysis based on first-principles calculations. The first striking difference comparing simple models with accurate *ab initio* data is prompted by the phonon dispersion in the unstrained case close to the Γ point, which in first-principles calculations present opposite curvatures for the two optical branches (see Fig. 3(b) of Ref. [48]). A simple force-constant model cannot catch this behavior based on only two parameters. From the same Fig. 3(b) of Ref. [48], we can estimate a phonon dispersion for the optical branches $\omega_4(\mathbf{q}) = \omega_{\mathrm{opt}} + A|\mathbf{q}|^2$, $\omega_3(\mathbf{q}) = \omega_{\mathrm{opt}} - B|\mathbf{q}|^2$, with $A = 25$ cm^{-1}/Å^2, $B = 80$ cm^{-1}/Å^2.

Furthermore, the actual experimental scenario suggests for few-layer h-BN, a strain-induced splitting rate ≈13 cm^{-2}/% [51], resulting for $\varepsilon = 2\%$ in a corresponding splitting at the Γ point $\Delta\omega_{\mathrm{opt}}(\Gamma) \approx 26$ cm^{-1}, one order of magnitude larger than the prediction of the simple model. Similarly, using these realistic values, we get $|\mathbf{Q}| = 0.5$ Å^{-1}. The present analysis thus suggests that, using monolayer h-BN as an example, the energies of the strain-induced changes in the optical spectra and the predicted momentum of the chiral phonons can be much larger in realistic materials than in the simple modeling using few force-constant parameters. The relevant energy scale of the chiral modes is expected to also be larger in TMDs, where the larger mass difference between the sublattices emphasized the chiral features. A detailed analysis of the strain-induced chiral phonon based on density-functional theory (DFT) calculations lie outside the aims of the present paper that has been focused on revealing the fundamental physics underlying. Future investigations using *ab initio* techniques are thus encouraged and welcome.

It is also worth discussing the possible ways for detecting and manipulating these chiral modes appearing close to the zone center. In this direction, a key role is played by the magnitude of the gap between the chiral modes $\Delta\omega_{\mathrm{chi}}$, taking into account different materials (h-BN, TMDs, etc.) and different theoretical (model-based or DFT-based) analyses, can range from fractions of cm^{-1} to few cm^{-1}. A direct spectroscopy probe of the chiral modes can thus be feasible in the latter case, whereas it is probably challenging for more conservative estimates. Further promising scenarios can come from near-field optical techniques, where finite $\mathbf{q}$ optical excitations can be launched, and couple to the chiral phonons considered here. Tuning the near-field conditions to better probe $\mathbf{q} \approx \mathbf{Q}_\alpha$, with a circularly polarized light, might be efficient in selectively exciting phonon modes with a specific chirality.

Besides the spectroscopy insights, an alternative path for detecting the role of these chiral modes is through their impact on macroscopic quantities. It should be noticed indeed that, due to such chiral modes, the system acquires a finite chiral wave vector defined as

$$\bar{\mathbf{Q}} = \sum_{\lambda, i=\pm} \mathbf{Q}_i s_{z,\lambda}(\mathbf{Q}_i) n_{\mathrm{B}}(\omega_\lambda(\mathbf{Q}_i)/T), \tag{46}$$

where, we remind, λ is the branch index, $i = \pm$ identifies the location in the Brillouin zone of the paired chiral phonons, and n_{B} is the Bose-Einstein thermal factor. This is significantly different from the chiral modes at the K points in the absence of strain where the threefold symmetry enforces $\bar{\mathbf{Q}} = 0$. The temperature thus has a crucial role ruling the finite but different populations of the gapped chiral modes for a given $\mathbf{Q}_i$. Simulating MoS_2 with characteristic phonon energies of optical phonon about ∼390 cm^{-1}, a hypothetical splitting of the chiral modes of 10 cm^{-1} would give at room temperature ($T = 300$ K) a difference in the population Δn_{B} of the opposite chiral modes of about $\Delta n_{\mathrm{B}} \sim 1\%$. This rate increases, however, at $\Delta n_{\mathrm{B}} \sim 5\%$, within the range of possible experimental observation. Such an estimate thus suggests the possibility of triggering chiral properties under nonequilibrium pump-probe ultrafast conditions, where a selective huge nonthermal population of phonons (hot phonons) with effective temperature $T_{\mathrm{hot}} \sim 1000$ K can be induced due to preferential electron-phonon channels. A common trait of two-dimensional hexagonal materials is indeed that the pump-induced energy, initially stored, in the electronic degrees of freedom, can be quickly transferred to few lattice modes, corresponding to intravalley and intervalley scattering. Those modes (including $\mathbf{Q}_\alpha$) can thus get *hot*, with effective temperatures that can reach the order of 10^3 K, making the possibility of probing the effects of a finite $\bar{\mathbf{Q}}$ more accessible. The occurrence of hot phonons in graphenes/graphite has already been assessed, and h-BN and TMDs are among the best candidates for similar physics [52–58].

A final mention concerning the possible ways of probing these (strain-driven) chiral phonons at small $\mathbf{q}'$s is through their effect on the acoustic modes. As discussed above, at $\mathbf{Q}_\alpha$ the physics of the avoided crossing point is strictly reflected in the optical branches, inducing modes with opposite chiralities $s_{z,3/4}(\mathbf{Q}_\alpha) \approx \pm 1$. However, a small but sizable chirality

content is also present at $\mathbf{Q}_\alpha$ in the acoustic branches, with $s_{z,1}(\mathbf{Q}_\alpha) \approx -0.16$ and $s_{z,2}(\mathbf{Q}_\alpha) \approx 0.15$, with a net $s_{z,1}(\mathbf{Q}_\alpha) + s_{z,2}(\mathbf{Q}_\alpha) \approx -0.01$. Although less strong than in the optical branches, keep in mind that such difference applies to modes that are *strongly* nondegenerate. Furthermore, the low-energy of the acoustic lattice modes makes them thermally populated and highly relevant for transport properties. The strain-induced chirality might thus be feasibly probed through the macroscopical effects related to the small but finite chiral content of the acoustic modes.

VII. SUMMARY

We utilize lattice deformation to break the threefold symmetry of hexagonal 2D material. This induces a band inversion in optical phonon bands, forming a chiral phonon mode near the zone center. We discuss the implication of strain in controlling the location of the chiral mode and its chiral strength. Our study can attract the interest of condensed matter researchers from different fields such as 2D systems, topological materials, strain engineering, topological thermal transport, etc. Our work highlights the importance of lattice deformations in manipulating phonon bands and, in particular, how strain can represent a suitable tool for controlling topological and geometrical (e.g., Berry curvature and orbital angular momentum) properties of phonons. This paper can motivate many investigations of strain on topological phonons in 2D materials and their heterostructures. The field of chiral phonon is developing very fast and we expect a rapid extension of the field along with the strain-driven effect on phonon dynamics.

ACKNOWLEDGMENTS

This work was supported by Nordita and the Swedish Research Council (No. VR 2018-04252). F.G. acknowledges funding from the European Commission, under the Graphene Flagship, Core 3, Grant No. 881603, and by Grants No. NMAT2D (Comunidad de Madrid, Spain), SprQuMat, and No. SEV-2016-0686, (Ministerio de Ciencia e Innovación, Spain). Nordita is partially supported by Nordforsk.

[1] K. Novoselov, A. Geim, S. Morozov, D. Jiang, Y. Zhang, S. Dubonos, I. Grigorieva, and A. Firsov, Science **306**, 666 (2004).
[2] K. Novoselov, D. Jiang, F. Schedin, T. Booth, V. Khotkevich, S. Morozov, and A. Geim, Proc. Natl. Acad. Sci. USA **102**, 10451 (2005).
[3] K. F. Mak, C. Lee, J. Hone, J. Shan, and T. F. Heinz, Phys. Rev. Lett. **105**, 136805 (2010).
[4] A. Splendiani, L. Sun, Y. Zhang, T. Li, J. Kim, C.-Y. Chim, G. Galli, and F. Wang, Nano Lett. **10**, 1271 (2010), pMID: 20229981.
[5] S. Z. Butler, S. M. Hollen, L. Cao, Y. Cui, J. A. Gupta, H. R. Gutiérrez, T. F. Heinz, S. S. Hong, J. Huang, A. F. Ismach, E. Johnston-Halperin, M. Kuno, V. V. Plashnitsa, R. D. Robinson, R. S. Ruoff, S. Salahuddin, J. Shan, L. Shi, M. G. Spencer, M. Terrones, W. Windl, and J. E. Goldberger, ACS Nano **7**, 2898 (2013).
[6] P. Ajayan, P. Kim, and K. Banerjee, Phys. Today **69**(9), 38 (2016).
[7] X. Li, L. Tao, Z. Chen, H. Fang, X. Li, X. Wang, J.-B. Xu, and H. Zhu, Appl. Phys. Rev. **4**, 021306 (2017).
[8] M. Vozmediano, M. Katsnelson, and F. Guinea, Phys. Rep. **496**, 109 (2010).
[9] S. Bertolazzi, J. Brivio, and A. Kis, ACS Nano **5**, 9703 (2011).
[10] R. Roldán, A. Castellanos-Gomez, E. Cappelluti, and F. Guinea, J. Phys.: Condens. Matter **27**, 313201 (2015).
[11] B. Amorim, A. Cortijo, F. de Juan, A. Grushin, F. Guinea, A. Gutiérrez-Rubio, H. Ochoa, V. Parente, R. Roldán, P. San-Jose, J. Schiefele, M. Sturla, and M. Vozmediano, Phys. Rep. **617**, 1 (2016).
[12] A. H. Castro Neto, F. Guinea, N. M. R. Peres, K. S. Novoselov, and A. K. Geim, Rev. Mod. Phys. **81**, 109 (2009).
[13] S. Tarasenko and E. Ivchenko, Jetp Lett. **81**, 231 (2005).
[14] A. Rycerz, J. Tworzydlo, and C. Beenakker, Nat. Phys. **3**, 172 (2007).
[15] T. Ando, Y. Zheng, and H. Suzuura, J. Phys. Soc. Jpn. **71**, 1318 (2002).
[16] D. Xiao, W. Yao, and Q. Niu, Phys. Rev. Lett. **99**, 236809 (2007).
[17] D. Xiao, M.-C. Chang, and Q. Niu, Rev. Mod. Phys. **82**, 1959 (2010).
[18] T. Ando, J. Phys. Soc. Jpn. **84**, 114705 (2015).
[19] L. Zhang and Q. Niu, Phys. Rev. Lett. **112**, 085503 (2014).
[20] L. Zhang and Q. Niu, Phys. Rev. Lett. **115**, 115502 (2015).
[21] H. Zhu, J. Yi, M.-Y. Li, J. Xiao, L. Zhang, C.-W. Yang, R. A. Kaindl, L.-J. Li, Y. Wang, and X. Zhang, Science **359**, 579 (2018).
[22] H. Chen, W. Zhang, Q. Niu, and L. Zhang, 2D Mater. **6**, 012002 (2019).
[23] W. Zhang, A. Srivastava, X. Li, and L. Zhang, Phys. Rev. B **102**, 174301 (2020).
[24] H. Komiyama and S. Murakami, Phys. Rev. B **103**, 214302 (2021).
[25] H. Chen, W. Wu, J. Zhu, S. A. Yang, and L. Zhang, Nano Lett. **21**, 3060 (2021).
[26] A. Ptok, A. Kobiałka, M. Sternik, J. Łażewski, P. T. Jochym, A. M. Oleś, S. Stankov, and P. Piekarz, Phys. Rev. B **104**, 054305 (2021).
[27] H. Pirie, S. Sadhuka, J. Wang, R. Andrei, and J. E. Hoffman, Phys. Rev. Lett. **128**, 015501 (2022).
[28] The possible onset of chiral phonons on a square lattice has been discussed in Wang *et al.*, arXiv:2111.05010.
[29] J. Sonntag, S. Reichardt, B. Beschoten, and C. Stampfer, Nano Lett. **21**, 2898 (2021).
[30] M. Huang, H. Yan, C. Chen, D. Song, T. F. Heinz, and J. Hone, Proc. Natl. Acad. Sci. USA **106**, 7304 (2009).
[31] T. M. G. Mohiuddin, A. Lombardo, R. R. Nair, A. Bonetti, G. Savini, R. Jalil, N. Bonini, D. M. Basko, C. Galiotis, N. Marzari,

K. S. Novoselov, A. K. Geim, and A. C. Ferrari, Phys. Rev. B **79**, 205433 (2009).
[32] Y. Wang, C. Cong, C. Qiu, and T. Yu, Small **9**, 2857 (2013).
[33] D. Doratotaj, J. R. Simpson, and J.-A. Yan, Phys. Rev. B **93**, 075401 (2016).
[34] S. Timoshenko and S. Woinowsky-Krieger, *Theory of Plates and Shells* (Mc Graw Hill, New York, 2010)
[35] To correctly consider the branch cut, one should intemperate $\arctan(y/x) = \arctan 2(x, y) = -i \ln[(x + iy)/\sqrt{x^2 + y^2}]$.
[36] P.-O. Löwdin, On the nonorthogonality problem, in *Advances in Quantum Chemistry*, edited by P.-O. Löwdin (Academic Press, 1970), Vol. 5, pp. 185–199.
[37] H. Wang, Y. Wang, X. Cao, M. Feng, and G. Lan, J. Raman Spectrosc. **40**, 1791 (2009).
[38] K. H. Michel and B. Verberck, Phys. Rev. B **80**, 224301 (2009).
[39] D. Sánchez-Portal and E. Hernández, Phys. Rev. B **66**, 235415 (2002).
[40] C. L. Kane and E. J. Mele, Phys. Rev. Lett. **78**, 1932 (1997).
[41] H. Suzuura and T. Ando, Phys. Rev. B **65**, 235412 (2002).
[42] K.-i. Sasaki, Y. Kawazoe, and R. Saito, Prog. Theor. Phys. **113**, 463 (2005).
[43] E. Mariani, A. J. Pearce, and F. von Oppen, Phys. Rev. B **86**, 165448 (2012).
[44] H. Rostami and R. Asgari, Phys. Rev. B **88**, 035404 (2013).
[45] H. Rostami, R. Roldán, E. Cappelluti, R. Asgari, and F. Guinea, Phys. Rev. B **92**, 195402 (2015).
[46] R. Geick, C. H. Perry, and G. Rupprecht, Phys. Rev. **146**, 543 (1966).
[47] S. Reich, A. C. Ferrari, R. Arenal, A. Loiseau, I. Bello, and J. Robertson, Phys. Rev. B **71**, 205201 (2005).
[48] Q. Cai, D. Scullion, A. Falin, K. Watanabe, T. Taniguchi, Y. Chen, E. J. G. Santos, and L. H. Li, Nanoscale **9**, 3059 (2017).
[49] A. Molina-Sánchez, K. Hummer, and L. Wirtz, Surf. Sci. Rep. **70**, 554 (2015).
[50] X. Zhang, X.-F. Qiao, W. Shi, J.-B. Wu, D.-S. Jiang, and P.-H. Tan, Chem. Soc. Rev. **44**, 2757 (2015).
[51] E. Blundo, E. Cappelluti, M. Felici, G. Pettinari, and A. Polimeni, Appl. Phys. Rev. **8**, 021318 (2021).
[52] S. Butscher, F. Milde, M. Hirtschulz, E. Malić, and A. Knorr, Appl. Phys. Lett. **91**, 203103 (2007).
[53] S. Berciaud, M. Y. Han, K. F. Mak, L. E. Brus, P. Kim, and T. F. Heinz, Phys. Rev. Lett. **104**, 227401 (2010).
[54] L. Huang, B. Gao, G. Hartland, M. Kelly, and H. Xing, Surf. Sci. **605**, 1657 (2011).
[55] M. Scheuch, T. Kampfrath, M. Wolf, K. von Volkmann, C. Frischkorn, and L. Perfetti, Appl. Phys. Lett. **99**, 211908 (2011).
[56] S. Wu, W.-T. Liu, X. Liang, P. J. Schuck, F. Wang, Y. R. Shen, and M. Salmeron, Nano Lett. **12**, 5495 (2012).
[57] D. Golla, A. Brasington, B. J. LeRoy, and A. Sandhu, APL Mater. **5**, 056101 (2017).
[58] Z. Chi, H. Chen, Q. Zhao, and Y.-X. Weng, Nanotechnology **31**, 235712 (2020).